Published in final edited form as:

Nature. 2009 January 22; 457(7228): 446–450. doi:10.1038/nature07637.

Inter-Subunit Coordination in a Homomeric Ring-ATPase

Jeffrey R. Moffitt[1,§], **Yann R. Chemla**[1,‡,§], **K. Aathavan**[2], **Shelley Grimes**[3], **Paul J. Jardine**[3], **Dwight L. Anderson**[3,4], and **Carlos Bustamante**[1,2,5,*]

[1]Department of Physics and Jason L. Choy Memorial Laboratory of Single-Molecule Biophysics, Berkeley, CA 94720

[2]Biophysics Graduate Group, University of California, Berkeley, CA 94720

[3]Department of Diagnostic and Biological Sciences, University of Minnesota, Minneapolis, MN 55455

[4]Department of Microbiology, University of Minnesota, Minneapolis, MN 55455

[5]Departments of Molecular and Cell Biology, Chemistry, and Howard Hughes Medical Institute, University of California, Berkeley, CA 94720

Abstract

Homomeric ring-ATPases perform many vital and varied tasks in the cell, ranging from chromosome segregation to protein degradation. Here we report the first direct observation of the inter-subunit coordination and the step size of such a ring-ATPase, the dsDNA packaging motor in the bacteriophage ϕ29. Using high-resolution optical tweezers, we find that packaging occurs in increments of 10 bp. Statistical analysis of the preceding dwell times reveals that multiple ATPs bind during each dwell, and application of high force reveals that these 10-bp increments are composed of four 2.5-bp steps. These results indicate that the hydrolysis cycles of the individual subunits are highly coordinated via a mechanism novel for ring-ATPases. In addition, a step size that is a non-integer number of base pairs demands new models for motor-DNA interactions.

Introduction

Multimeric ring-ATPases of the ASCE (Additional Strand, Conserved E) superfamily represent a structurally homologous yet functionally diverse group of proteins involved in such varied tasks as ATP synthesis, protein unfolding and degradation, and DNA translocation1-5. Despite their importance, the coordination mechanism between the

*Correspondence should be addressed to C.B. (carlos@alice.berkeley.edu.).

‡Present Address: Departments of Physics and Biophysics, University of Illinois, Urbana-Champaign, Urbana, IL 61801

§J.R.M. and Y.R.C. contributed equally to this work.

J.R.M., Y.R.C, and K.A. conducted the experiments and performed the analysis, S.G., P.J.J., and D.A. prepared and provided experimental materials, and J.R.M, Y.R.C., K.A., S.G., P.J.J., D.A., and C.B. wrote the paper.

Supplementary Information accompanies the paper at www.nature.com/nature.

The authors declare no competing financial interests.

hydrolysis cycles of the individual and often identical subunits that compose these ringed-proteins is poorly understood. Recent crystallographic and bulk biochemical studies2, 4 suggest various models of coordination in which subunits act sequentially and in order6-14, simultaneously and in concert15, or independently and at random16. Unfortunately, direct observation of subunit dynamics has only been reported for a heteromeric system, the F1 ring of ATP synthase8, whose heterodimers function in a sequential manner.

The DNA packaging motor in the *Bacillus subtilis* bacteriophage ϕ29 provides a model system to investigate the inter-subunit coordination in homomeric ring-ATPases because it can be fully reconstituted *in vitro*17, it has a relatively slow translocation rate18, 19, and it has been extensively characterized by bulk20 and single-molecule18, 19, 21-23 methods. Packaging of the double-stranded DNA genome of ϕ29 into its proteinaceous precursor capsid (prohead) is driven by a powerful molecular machine18 which consists of three multimeric rings organized coaxially around the point of DNA entry20: a dodecameric24 ring of gene product 10 (gp10) known as the head-tail connector, a pentameric24-26 ring of RNA molecules known as the prohead-RNA (pRNA), and a pentameric24, 26 ring of the ATPase gp16 (see Figure 1a). Sequence homology27 places gp16 in the FtsK/HerA family of dsDNA translocases28. This family is itself a member of the large ASCE superfamily, thus relating the packaging motor to the ubiquitous AAA+ and RecA-like proteins3, 5.

Recent studies of the packaging motor have suggested a mechanism in which the subunits operate sequentially19, each binding ATP, hydrolyzing it, and translocating the DNA by 2 bp19, 29, before the next subunit repeats this cycle. While this scheme is consistent with the observed data19, 24, 30 and with sequential models proposed for other ring-ATPases2, 4, 6-14, direct observation of the coordination of the mechanochemical cycles of the individual subunits in the packaging motor is still lacking. In this article, we report the first measurements of the individual packaging steps of the ϕ29 motor, which reveal both its step size and the novel coordination between its subunits. Because of its relation to the ASCE superfamily27, the mechanism for the packaging motor we propose here may have implications for the function of a diverse set of ring-ATPases.

DNA is Packaged in 10-bp Increments

To probe the dynamics of the packaging motor of ϕ29, single prohead-motor-DNA complexes are tethered between two 860-nm diameter polystyrene beads held in two optical traps as in Figure 1a. Packaging is initiated *in situ*22, 23 or by restarting stalled complexes18, 19 in an ATP packaging buffer and monitored in a semi-passive mode in which the tension applied to the motor is kept within a narrow range by periodically changing the distance between the two traps (Supplementary Figure 1). Motor translocation is determined from the decrease in the contour length of the DNA tether and is followed with base-pair-scale resolution31-33.

In our first experiments we probe packaging at an average low external tension of ∼ 8 pN, and at ATP concentrations ([ATP]) above and below the K_M of the motor, ∼30 μM19. Figure 1b shows representative packaging traces collected under these conditions. Across the full range of [ATP], packaging of DNA occurs in a stepwise manner consisting of

"dwells," in which the DNA length remains constant, followed by "bursts," in which DNA is translocated in ∼10-bp increments. We determine the average length of DNA encapsidated in these packaging bursts for each [ATP] from the periodicity in the average pairwise distance distribution (PWD) as seen in Figure 1c. No statistically significant trend is observed in the size of these bursts as a function of [ATP] (see Figure 1d); thus, the average of these values, 10.0 ± 0.2 bp (s.d.), is the best estimate for the burst size.

To elucidate the mechanism by which the motor translocates in 10-bp increments, we analyze the time the motor spends in the dwell before each burst and the time it takes to complete each burst as a function of [ATP]. Figure 2a shows the distribution of dwell times before the packaging bursts. The mean dwell time, seen in Figure 2b, shows a strong dependence on [ATP] that follows an inverse hyperbolic expression, $\langle \tau \rangle = (K_{1/2} + [T])/(k_{cat}[T])$, with a $K_{1/2}$ of 23 ± 7 μM (s.d.) and a k_{max} of 8.7 ± 0.7 s^{-1} (s.d.). In contrast, Figure 2b shows that the average duration of the packaging burst has little or no dependence on [ATP], suggesting that ATP binding occurs only in the dwells and not in the bursts. Taken together these observations produce a packaging velocity with a Michaelis-Menten [ATP] dependence consistent with previous measurements19.

The specific shape of the dwell time distributions seen in Figure 2a provides further information on the kinetic transitions within a single dwell. In particular, the more sharply peaked the distribution, the larger the number of rate-limiting kinetic transitions that compose the dwell34. We quantify the degree to which these distributions are peaked with the ratio of the squared mean of the dwell times to their variance, the inverse of the randomness parameter34 (Figure 2c). It can be shown that this parameter, n_{min}, provides a strict lower bound35 on the number of rate-limiting transitions under each [ATP] that occur during the dwell.

At limiting [ATP], 5 μM << K_M, we measure an n_{min} of 2.0 ± 0.4 (s.e.m), indicating that there are at least two rate-limiting transitions in each dwell. Since ATP binding must be rate-limiting under these conditions, we conclude that no less than 2 ATP molecules bind to the motor before each 10-bp burst. (In contrast, if a single ATP were to bind during each dwell, one would expect the dwell time distribution to be a single exponential and n_{min} to be 1)34, 36. At saturating [ATP], 1 mM >> K_M, we measure an n_{min} of 3.8 ± 0.5 (s.e.m.). Since binding is no longer rate-limiting, this indicates that at least 4 additional non-binding transitions must occur in each dwell. For intermediate [ATP], both binding and non-binding transitions can be rate-limiting; thus, we expect n_{min} to peak to a value greater than either of the extreme values, exactly as is observed. Thus, Figure 2c indicates that in total no less than 6 kinetic transitions must occur in the dwell before each 10-bp burst—at least 2 ATP binding events and at least 4 non-binding transitions.

Packaging Occurs in Four 2.5-bp Steps

The findings that packaging occurs in 10-bp increments—five times larger than the 2-bp value proposed from bulk measurements19, 29 —and that the preceding dwells contain multiple ATP binding transitions suggest that the 10-bp bursts may be composed of multiple smaller steps that in general may be too fast to resolve under the above conditions. This

inference is supported by the observation that many bursts have durations larger than the measurement bandwidth (Figure 1b and Figure 2b), indicative of intermediate kinetic transitions. Supplementary Figure 4 shows that occasionally these intermediate transitions can be resolved, appearing as short micro-dwells that split the 10-bp burst into smaller steps. A correlation analysis36 confirms that these smaller steps occur in groups that add to 10 bp, ruling out the possibility that these events represent a variable burst size (Supplementary Discussion).

As a direct demonstration of the composition of the 10-bp bursts, we follow packaging against high external loads at near-saturating [ATP] (250 μM). Since translocation steps correspond to force-generating kinetic transitions, we expect that the duration of the micro-dwells preceding these steps will increase with increasing external force37. Figure 3a shows that, under 40 pN of average load, smaller steps of ∼2.5 bp and integer multiples thereof can be clearly and frequently observed. The PWD for this data, shown in Figure 3b, reveals a periodicity of 2.4 ± 0.1 bp (s.d.) and the step size distribution, shown in Supplementary Figure 6, has a peak at 2.48 ± 0.03 bp (s.e.m.). The inset to Figure 3b shows that the periodicity in the PWD is independent of force, indicating that the 2.5-bp step size is a constant feature of the motor and that the 10-bp bursts observed at low force are composed of four 2.5-bp steps. This conclusion is further supported by the prominent fourth peak observed in the PWD which is consistent with the corresponding 10-bp periodicity observed at low force.

The dwell time distribution associated with the 2.5-bp steps (Figure 3c) is well described by a weighted sum of two exponential decays, with a fast rate of 22 ± 2 s^{-1} (s.d.) and a slow rate of 8 ± 1 s^{-1} (s.d.). The fast rate rationalizes the fraction of 2.5-bp steps that are missed in our analysis and the slow rate is consistent with one out of every four dwells coming from the same peaked dwell time distribution observed at low force (Supplementary Figures 5 and 6). Finally, our data do not support alternative interpretations of the 2.5-bp periodicity, such as distortions from B-form or alternating integer steps, as discussed in Supplementary Figures 7 and 8 and in the Supplementary Discussion, though some variability in the step size on the ∼0.1-bp scale cannot be ruled out.

Inter-Subunit Coordination

Taken together these results indicate that the mechanochemical cycles of the identical subunits of the packaging motor of ϕ29 are highly coordinated, with the loading of ATP and the translocation of DNA segregated into two distinct phases that comprise the mechanochemical cycle of the entire ring (Figure 4a). During the initial, “dwell,” phase the DNA is held at constant length while multiple ATPs are loaded, giving this dwell its observed [ATP] dependence (Figure 2). This process is followed by the “burst” phase in which DNA is packaged in four increments of 2.5 bp, totaling 10 bp of DNA translocated per cycle (Figures 1d and 3b). Thus, this phase has an average duration that is independent of [ATP] but dependent on force (Figures 2b and 3c).

The observation of four translocation steps per burst strongly suggests that four ATPs bind to the ring each dwell, one for each of the subsequent steps in the burst phase. This inference

is consistent with the measured value of n_{min} at limiting [ATP] since reversibility in binding or differences in binding rates will decrease the observed value of n_{min} from the actual number of binding events34. It is also consistent with the 10-bp burst size since a single ATP provides insufficient free energy to package 10-bp against the high forces tested previously18, 19, 37. Moreover, the binding of four ATPs predicts a coupling constant between ATP consumption and packaging of 2.5 bp/ATP, in reasonable agreement with the ∼2 bp/ATP value estimated from bulk measurements19, 29. The ∼25% discrepancy may be explained by additional processes that consume ATP in bulk measurements, such as the repackaging of DNA that slips from the capsid18, 19. However, it is also possible that a regulatory fifth ATP is bound each cycle and hydrolyzed futilely.

Our data also restrict the possible mechanisms by which these ATPs bind to the ring. The requirement that multiple substrate molecules bind per cycle typically results in a sigmoidal dependence on [ATP]38—the hallmark of binding cooperativity. Yet previous velocity measurements19 and the mean dwell times measured here (Figure 2b) are well described by a simple, non-sigmoidal ATP dependence. Since a sigmoidal [ATP] dependence arises whenever two or more binding events are connected reversibly38, these two observations can be reconciled if and only if the binding of each ATP is separated from the other binding events by a largely irreversible transition. In this case the mean dwell time will display a non-sigmoidal [ATP] dependence despite the cooperative binding of ATP (Supplementary Discussion). This requirement is consistent with previous observations for ϕ2919 and related ring-ATPases39 which indicate that binding occurs in at least two kinetic steps – (1) a reversible “docking” transition in which the molecule comes in weak contact with the catalytic pocket followed by (2) a largely irreversible “tight-binding” transition39 in which ATP makes a stronger contact to the binding site and is committed to the hydrolysis cycle (Figure 4b). More intermediate kinetic states in ATP binding are also possible, but are not required to explain our observations.

In addition, the non-sigmoidal [ATP] dependence of the mean dwell times also restricts the temporal order in which the subunits can dock ATP. Kinetic schemes in which multiple subunits are capable of reversibly docking ATP simultaneously will necessarily have a sigmoidal [ATP] dependence because such schemes have binding events that are reversibly connected38 (Supplementary Discussion.) Thus, it is not sufficient to require that each loose docking of ATP be followed by a tight-binding transition; we must also require that only one subunit at a time can be involved in ATP docking. The simplest model that produces this time-ordered docking is one in which the tight-binding transition of one subunit allosterically activates the binding pocket of another subunit, making it competent to dock ATP, a process depicted in Figure 4c (Supplementary Discussion). While our data cannot uniquely determine the actual sequence in which the subunits bind ATP, this required allosteric activation in combination with the known interfacial interactions of adjacent subunits in related ring-ATPases3, 5 strongly favors a mechanism in which successive ATP binding occurs in a sequential and *ordinal* fashion around the ring as depicted in Figure 4.

Figure 4d summarizes the kinetic transitions that occur during a complete mechanochemical cycle of the packaging motor. During the binding phase, four ATPs bind to the ring in the two-step process depicted in Figure 4b and c. Previous work has shown that the release of

phosphate precedes or coincides with translocation19. Thus, after the ring has bound four ATPs, the burst phase is triggered, the first phosphate is released, and the first 2.5-bp step is taken. The burst phase then proceeds with three additional 2.5-bp steps preceded by three force dependent micro-dwells. The number of rate-limiting steps, n_{min}, at saturating ATP (Figure 2c) indicates that multiple kinetic transitions besides ATP binding must occur during the dwell phase. These transitions may correspond to the hydrolysis of the bound ATPs or the release of multiple ADPs from the previous cycle or, perhaps, both. Moreover, these transitions may occur together either as trigger or reset processes (Figure 4d) or interspersed between ATP binding events. It is also possible that these additional events correspond to the tight-binding transitions, though this is unlikely given that tight-binding is believed to occur quite rapidly19.

The two-phase model we propose here is also consistent with previous measurements of the packaging motor18, 19. For example, it has been shown that the binding of a single non-hydrolyzable ATP analog is sufficient to pause the entire motor19—a result consistent with the high degree of inter-subunit coordination observed here. Furthermore, a biphasic sedimentation profile observed in sucrose gradient experiments suggests the ability of the ring to load multiple nucleotides19, consistent with our model. Finally, the two-phase model predicts the same dependence of the packaging velocity with force and [ATP] as observed previously18, 19.

Non-Integer Step Size Models

Our finding that packaging occurs in four 2.5-bp translocation steps raises two notable questions on the motor mechanism. First, how does a dsDNA translocase move in a non-integer number of base pairs? And, second, how is the pentameric symmetry24-26 of the motor broken, generating only four steps per cycle? A step size that is a non-integer number of base pairs prohibits any mechanism in which every motor subunit within a closed ring makes specific and identical chemical contacts with one strand of the DNA. Under this constraint, we can speculate on several alternative mechanisms that would produce a 2.5-bp step size and the implications these models have for a pentameric motor.

A non-integer step size could be generated if each subunit is capable of binding two or more alternating chemical moieties, which may or may not be on the same strand. Alternatively, the motor may make no specific contacts, but rather drive translocation via steric interactions, in which case the step size would be set not by the chemical periodicity of the DNA but by the size of the internal conformational changes that generate the power stroke. One example of such a mechanism is depicted in Figure 5a where each subunit makes non-specific contacts with the major groove of the DNA. In such a model, generation of four translocation steps requires that one of the five subunits is not equivalent to the other four, breaking the symmetry of the pentameric ring. Since the nucleotide-free state is disengaged from the DNA19, one subunit may be required to retain nucleotide at the end of the previous cycle, ensuring that a strong contact with the DNA is maintained while the remaining subunits load ATP during the subsequent dwell phase.

Alternatively, a single specific chemical contact may be made with the DNA but not with every subunit. In this class of models, only a subset of the subunits interact with the DNA and relative motion between these subunits is what drives translocation. Figure 5b depicts an example of such a mechanism in which only two subunits make specific contact with the DNA. Translocation is achieved via an “inchworm-like” movement of these two subunits driven by distortions in the ring. One appeal of this mechanism is that because a single specific contact is made with the DNA, it produces an integer burst size, yet because the DNA-binding subunits are retracted by conformational changes induced into the ring by the other subunits, this burst can be divided into non-integer steps. Moreover, this model also explains naturally the observation of four steps by a pentameric motor since one subunit interface must bear the accumulated distortion of the other four subunits, perhaps inactivating one of the five binding pockets. The relative motion between adjacent subunits needed to accommodate such a mechanism has been observed in the crystal structures of other ring-ATPases6, 40 but has not been implicated as part of the translocation mechanism41. Future measurements will be aimed at testing the spectrum of models discussed here.

Conclusions

We have presented here the first high-resolution measurements of the stepping dynamics of the ring-ATPase of the packaging motor of bacteriophage ϕ29. Our results indicate a highly coordinated two-phase mechanism in which the binding of ATP and the translocation of DNA by multiple subunits are organized into two distinct and temporally segregated portions of the mechanochemical cycle of the ring. Our observation of a 2.5-bp step size challenges the long-held view that DNA translocation must occur in integer base pair increments, making it necessary to devise new and more complex models for motor-DNA interactions. In addition, while the inter-subunit coordination we observe is reminiscent of aspects of both the concerted-action model of the large tumor antigen of SV4015 and the sequential models proposed for the translocases BPV E1, T7 gp4, φ12 P4, *E. coli* rho, and FtsK6, 7, 9-14, our mechanism represents a novel type of coordination not previously proposed for ring-ATPases. Provocatively, while a two-phase mechanisms contrasts with these other models, it appears to be consistent with many of the biochemical11-14 and structural6, 7, 9, 10, 13 observations made on these related systems. One notable exception is the ClpX protease for which biochemical data clearly suggest a limited degree of subunit coordination16. However, recent work on a related system, the archaeal MCM, suggests that coordinated systems can take alternative pathways when overcoming functional barriers such as catalytically inactive subunits42. Ring-ATPases of the ASCE superfamily support a large and remarkably diverse set of cellular functions by drawing upon a comparatively small set of common structural features. Direct measurements of the inter-subunit dynamics in these systems, such as those presented here, promise to reveal if these diverse cellular functions arise from a similarly small set of common structural dynamics.

Methods Summary

Complexes of prohead, gp16, and biotinylated DNA were prepared and attached to 860-nm polystyrene beads (Spherotech, Libertyville, IL) coated with antibodies to ϕ29 or

streptavidin using methods that have been described previously18, 19. Tethers were assembled and packaging was restarted in a packaging buffer (50 mM TrisHCl, 50 mM NaCl, 5 mM $MgCl_2$, 10 μg/mL BSA, 0.1% NaN_3, pH 7.8) supplemented with various amounts of ATP (Sigma-Aldrich, St. Louis, MO)18, 19. Experiments were conducted in two separate dual-trap instruments, built around two different trapping lasers32, 33, and calibrated using standard techniques32, 33, 43. The contour length of the DNA tether was calculated from the measured force and extension using the extensible worm-like-chain model as described previously18, 19. Pairwise distributions were calculated from data filtered with a sliding 20 ms box-car window as described previously44. The location and duration of stepping transitions were found with a t-test analysis similar to previous methods45. Dwell times were calculated directly from the time between transitions, and burst durations were calculated from the number of points within transitions. The mean and variance were calculated directly from these dwell times, and the errors were estimated using a bootstrap method. n_{min} was calculated directly from these moments34, 36.

Methods

Sample Preparation

Prohead, gp16, and genomic DNA were isolated as described previously47. For a stalled complex method of initiation18, 19, a ClaI (New England Biolabs, Ipswich, MA) digest of genomic DNA was biotinylated using Klenow exo- (New England Biolabs, Ipswich, MA) to fill in the overhang with biotinylated nucleotides (Sigma-Aldrich, St. Louis, MO) 18, 19. Preferential packaging of the left end of the genome20 favors the formation of prohead-motor-DNA complexes with the 6,149 bp fragment of the ClaI digest. Stalled complexes were then bound to antibody beads, made as described previously18, and introduced into the tweezers with streptavidin coated beads. For the *in situ* method of initiation22, 23, a 4,277 bp tether PCR amplified from lambda DNA with a biotinylated primer was bound to streptavidin coated beads, and stalled prohead-motor complexes22, 23 were bound to antibody beads. In both initiation methods, tethers were formed in the tweezers by physically bumping the two beads. The *in situ* initiation method was used for all [ATP] ≥ 25 μM since data were in general less noisy and easier to collect; however, a severe drop in tether formation efficiency below 25 μM required the use of the stalled complex method for low [ATP]. All tether lengths were selected to reduce the effect of packaged DNA on motor dynamics18, 23.

Optical Trapping Instruments

Two different optical trapping instruments were used in these studies32, 33. All low force data for 25 μM ≤ [ATP] ≤ 250 μM were collected using a instrument built around a 845-nm, 200 mW diode laser32. All other data were collected using an instrument built around a high-power, diode-pumped, solid-state 1064-nm laser33. Both instruments exploit the correlations in the motion of the two trapped beads with a differential detection technique32 to achieve base-pair-resolution on the second time scale31-33. Due to increased laser absorption at 1064-nm48, the high force data were collected in an 80% Deuterium-oxide (D2O) buffer to avoid heating effects caused by the high laser power needed to provide the large opposing forces. Supplementary Figure 5 shows that while D2O alters the kinetics of

packaging, it does not change the size of the packaging bursts. In addition, when working with the 1064-nm trapping laser, an oxygen scavenging system was added (100 μg/mL glucose oxidase, 20 μg/mL catalase, 5 mg/mL dextrose; Sigma-Aldrich, St. Louis, MO) to prevent the formation of the reactive species singlet oxygen.

Calibration

Traps were calibrated using the thermal fluctuations of the trapped beads43. The contour length was calculated from the measured extension and force with the extensible worm-like-chain model using a persistence length of 53 nm, a stretch modulus of 1200 pN19, 49, and an average B-form DNA rise of 3.4 Å/bp50. Distance calibrations were corroborated with video microscopy33, which was calibrated to 0.3% with two different distance standards (Nikon, Mellville, NY; Graticules, London) and confirmed to 1% by measuring the extension of DNA of different lengths, ∼1, 2, 3, and 5.6 kb. All packaging experiments were conducted in a semi-passive mode (Supplementary Figure 1), in which the trap separation was kept constant as packaging proceeded and was changed discretely to keep the tension within a set range, ∼6-10 pN for low force experiments and ∼33-46 pN for high force experiments. All reported data have been corrected for small systematic errors, ∼4% (Supplementary Figures 1 and 2), determined from the discrete changes in the trap separation as described in the Supplementary Discussion.

Analysis

The one-sided autocorrelation of a positional histogram of each semi-passive mode segment was used to calculate the pairwise distributions44. 0.25-bp bins and 0.1-bp bins were used for the histograms for the low force and high force distributions respectively. Data were selected for low noise and clarity of steps as described in the Supplementary Discussion. The pairwise distributions of the selected data were averaged together to produce the reported distributions. The average spatial periodicity was quantified from the position of the peaks. Subsets of the high force data were analyzed to produce the step size measurement as a function of force.

Stepping transitions were identified using a t-test analysis45 and a probability threshold of observing a given t-value of 10^{-4}. Dwell times were calculated from the time between transitions and step sizes were calculated from the difference in mean position between transitions. The reported dwell time distributions in Figure 2a and 3c were selected based on the size of the subsequent step, 8-12 bp and 1.5-4 bp respectively. Burst durations were estimated from the exponential decay rate of the distribution of the number of contiguous points for which the t-value probability was below the 10^{-4} threshold. Because of our limited time resolution, we could not observe the expected peak in this distribution; thus, we report the observed exponential decay, a value less biased by the time resolution than the mean. The effective bandwidth of the t-test algorithm was varied to maximize the number of observed steps while minimizing the systematic errors introduced into the moments of the distribution from a finite dead-time. By assuming a Poisson distribution, it was determined that this dead-time algorithm introduces negligible systematic errors in the calculated moments for all reported distributions.

Supplementary Material

Refer to Web version on PubMed Central for supplementary material.

Acknowledgments

We thank C. L. Hetherington, M. Nollmann, and G. Chistol for a critical reading of the manuscript; C. L. Hetherington, A. Politzer, M. Strycharska, M. Kopaczynska, and J. Yu for critical discussions; and J. Choy, S. Grill, and S. Smith for advice regarding instrumentation. J.R.M. acknowledges the National Science Foundation's Graduate Research Fellowship and Y.R.C. the Burroughs Welcome Fund's Career Awards at the Scientific Interface for funding. This research was supported in part by NIH grants GM-071552, DE-003606, and GM-059604. The content is solely the responsibility of the authors and does not necessarily represent the official views of the National Institutes of Health.

REFERENCES

1. Latterich M, Patel S. The AAA team: related ATPases with diverse functions. Trends in Cell Biology. 1998; 8:65. [PubMed: 9695811]
2. Ogura T, Wilkinson AJ. AAA+ superfamily ATPases: common structure--diverse function. Genes to Cells. 2001; 6:575–597. [PubMed: 11473577]
3. Iyer LM, Leipe DD, Koonin EV, Aravind L. Evolutionary history and higher order classification of AAA+ ATPases. J Struct Biol. 2004; 146:11–31. [PubMed: 15037234]
4. Kainov DE, Tuma R, Mancini EJ. Hexameric molecular motors: P4 packaging ATPase unravels the mechanism. Cell Mol Life Sci. 2006; 63:1095–105. [PubMed: 16505972]
5. Erzberger JP, Berger JM. Evolutionary relationships and structural mechanisms of AAA+ proteins. Annu Rev Biophys Biomol Struct. 2006; 35:93–114. [PubMed: 16689629]
6. Singleton MR, Sawaya MR, Ellenberger T, Wigley DB. Crystal structure of T7 gene 4 ring helicase indicates a mechanism for sequential hydrolysis of nucleotides. Cell. 2000; 101:589–600. [PubMed: 10892646]
7. Mancini EJ, et al. Atomic snapshots of an RNA packaging motor reveal conformational changes linking ATP hydrolysis to RNA translocation. Cell. 2004; 118:743–55. [PubMed: 15369673]
8. Kinosita K, Adachi K, Itoh H. ROTATION OF F1-ATPASE: How an ATP-Driven Molecular Machine May Work. Annual Review of Biophysics and Biomolecular Structure. 2004; 33:245–268.
9. Enemark EJ, Joshua-Tor L. Mechanism of DNA translocation in a replicative hexameric helicase. Nature. 2006; 442:270. [PubMed: 16855583]
10. Skordalakes E, Berger JM. Structural insights into RNA-dependent ring closure and ATPase activation by the Rho termination factor. Cell. 2006; 127:553–64. [PubMed: 17081977]
11. Adelman JL, et al. Mechanochemistry of Transcription Termination Factor Rho. Molecular Cell. 2006; 22:611. [PubMed: 16762834]
12. Liao J-C, Jeong Y-J, Kim D-E, Patel SS, Oster G. Mechanochemistry of T7 DNA Helicase. Journal of Molecular Biology. 2005; 350:452. [PubMed: 15950239]
13. Massey TH, Mercogliano CP, Yates J, Sherratt DJ, Löwe J. Double-Stranded DNA Translocation: Structure and Mechanism of Hexameric FtsK. Molecular Cell. 2006; 23:457. [PubMed: 16916635]
14. Crampton DJ, Mukherjee S, Richardson CC. DNA-induced switch from independent to sequential dTTP hydrolysis in the bacteriophage T7 DNA helicase. Mol Cell. 2006; 21:165–74. [PubMed: 16427007]
15. Gai D, Zhao R, Li D, Finkielstein CV, Chen XS. Mechanisms of conformational change for a replicative hexameric helicase of SV40 large tumor antigen. Cell. 2004; 119:47–60. [PubMed: 15454080]
16. Martin A, Baker TA, Sauer RT. Rebuilt AAA + motors reveal operating principles for ATP-fuelled machines. Nature. 2005; 437:1115. [PubMed: 16237435]
17. Guo P, Grimes S, Anderson D. A defined system for in vitro packaging of DNA-gp3 of the Bacillus subtilis bacteriophage phi 29. Proc Natl Acad Sci U S A. 1986; 83:3505–9. [PubMed: 3458193]

18. Smith DE, et al. The bacteriophage straight phi29 portal motor can package DNA against a large internal force. Nature. 2001; 413:748–52. [PubMed: 11607035]
19. Chemla YR, et al. Mechanism of force generation of a viral DNA packaging motor. Cell. 2005; 122:683–692. [PubMed: 16143101]
20. Grimes S, Jardine PJ, Anderson D. Bacteriophage phi 29 DNA packaging. Adv Virus Res. 2002; 58:255–94. [PubMed: 12205781]
21. Hugel T, et al. Experimental test of connector rotation during DNA packaging into bacteriophage phi29 capsids. PLoS Biol. 2007; 5:e59. [PubMed: 17311473]
22. Fuller DN, et al. Ionic effects on viral DNA packaging and portal motor function in bacteriophage phi 29. Proc Natl Acad Sci U S A. 2007; 104:11245–50. [PubMed: 17556543]
23. Rickgauer JP, et al. Portal motor velocity and internal force resisting viral DNA packaging in bacteriophage phi29. Biophys J. 2008; 94:159–67. [PubMed: 17827233]
24. Simpson AA, et al. Structure of the bacteriophage phi29 DNA packaging motor. Nature. 2000; 408:745–50. [PubMed: 11130079]
25. Morais MC, et al. Cryoelectron-microscopy image reconstruction of symmetry mismatches in bacteriophage phi29. J Struct Biol. 2001; 135:38–46. [PubMed: 11562164]
26. Morais MC, et al. Defining Molecular and Domain Boundaries in the Bacteriophage [phi]29 DNA Packaging Motor. Structure. 2008; 16:1267. [PubMed: 18682228]
27. Burroughs, AM.; Iyer, LM.; Aravind, L. Gene and Protein Evolution. Volff, J-N., editor. Karger; Basel: 2007. p. 48-65.
28. Iyer LM, Makarova KS, Koonin EV, Aravind L. Comparative genomics of the FtsK-HerA superfamily of pumping ATPases: implications for the origins of chromosome segregation, cell division and viral capsid packaging. Nucleic Acids Res. 2004; 32:5260–79. [PubMed: 15466593]
29. Guo P, Peterson C, Anderson D. Prohead and DNA-gp3-dependent ATPase activity of the DNA packaging protein gp16 of bacteriophage phi 29. J Mol Biol. 1987; 197:229–36. [PubMed: 2960820]
30. Chen C, Guo P. Sequential action of six virus-encoded DNA-packaging RNAs during phage phi29 genomic DNA translocation. J Virol. 1997; 71:3864–71. [PubMed: 9094662]
31. Moffitt JR, Chemla YR, Smith SB, Bustamante C. Recent Advances in Optical Tweezers. Annu Rev Biochem. 2008; 77:205–228. [PubMed: 18307407]
32. Moffitt JR, Chemla YR, Izhaky D, Bustamante C. Differential detection of dual traps improves the spatial resolution of optical tweezers. Proceedings of the National Academy of Sciences. 2006; 103:9006–9011.
33. Bustamante, C.; Chemla, YR.; Moffitt, JR. Single-Molecule Techniques: A Laboratory Manual. Selvin, PR.; Ha, T., editors. Cold Spring Harbor Laboratories; Cold Spring Harbor, New York: 2008. p. 297-324.
34. Schnitzer MJ, Block SM. Statistical kinetics of processive enzymes. Cold Spring Harbor Symposia on Quantitative Biology. 1995; 60:793–802. [PubMed: 8824454]
35. Koza Z. Maximal force exerted by a molecular motor. Physical Review E. 2002; 65:031905.
36. Chemla YR, Moffitt JR, Bustamante C. Exact Solutions for Kinetic Models of Macromolecular Dynamics. J. Phys. Chem. B. 2008; 112:6025–6044. [PubMed: 18373360]
37. Bustamante C, Chemla YR, Forde NR, Izhaky D. Mechanical processes in biochemistry. Annu Rev Biochem. 2004; 73:705–48. [PubMed: 15189157]
38. Segel, IH. Enzyme Kinetics. John Wiley & Sons, Inc.; 1975.
39. Oster G, Wang H. Reverse engineering a protein: the mechanochemistry of ATP synthase. Biochim Biophys Acta. 2000; 1458:482–510. [PubMed: 10838060]
40. Skordalakes E, Berger JM. Structure of the Rho transcription terminator: mechanism of mRNA recognition and helicase loading. Cell. 2003; 114:135–46. [PubMed: 12859904]
41. Lisal J, et al. Functional visualization of viral molecular motor by hydrogen-deuterium exchange reveals transient states. Nat Struct Mol Biol. 2005; 12:460–6. [PubMed: 15834422]
42. Moreau MJ, McGeoch AT, Lowe AR, Itzhaki LS, Bell SD. ATPase Site Architecture and Helicase Mechanism of an Archaeal MCM. Molecular Cell. 2007; 28:304. [PubMed: 17964268]

43. Berg-Sorensen K, Flyvbjerg H. Power spectrum analysis for optical tweezers. Review Of Scientific Instruments. 2004; 75:594–612.
44. Block SM, Svoboda K. Analysis of high resolution recordings of motor movement. Biophys. J. 1995; 68:2305S–2415.
45. Carter NJ, Cross RA. Mechanics of the kinesin step. Nature. 2005; 435:308. [PubMed: 15902249]
46. Parzen E. Estimation of a Probability Density-Function and Mode. Annals of Mathematical Statistics. 1962; 33:1065.
47. Grimes S, Anderson D. The bacteriophage phi29 packaging proteins supercoil the DNA ends. J Mol Biol. 1997; 266:901–14. [PubMed: 9086269]
48. Kellner L. The near infra-red absorption spectrum of heavy water. Proceedings of the Royal Society of London Series a-Mathematical and Physical Sciences. 1937; 159:0410–0415.
49. Baumann CG, Smith SB, Bloomfield VA, Bustamante C. Ionic effects on the elasticity of single DNA molecules. Proceedings of the National Academy of Sciences. 1997; 94:6185–6190.
50. Yanagi K, Prive GG, Dickerson RE. Analysis of local helix geometry in three B-DNA decamers and eight dodecamers. J Mol Biol. 1991; 217:201–14. [PubMed: 1988678]

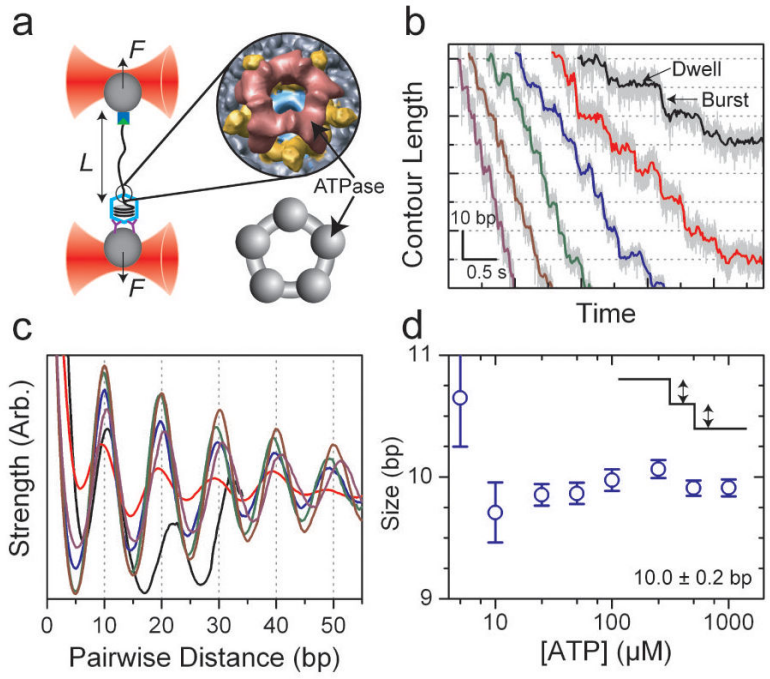

Figure 1. Bacteriophage ϕ29 Packages DNA in Bursts of 10 bp

(a) A single packaging bacteriophage prohead-motor complex and its dsDNA substrate are tethered between two beads each held in an optical trap. Inset: cryo-EM reconstruction of the full motor complex26 (Courtesy of M. Morais), ATPase in red, pRNA in yellow, connector in cyan, and capsid in gray with a top view cartoon of the ATPase ring alone (below, gray). (b) Representative packaging traces collected under low external load, ∼8 pN, and different [ATP]: 250 μM, 100 μM, 50 μM, 25 μM, 10 μM, and 5 μM in purple, brown, green, blue, red, and black, respectively, all boxcar-filtered and decimated to 50 Hz. Data at 1.25 kHz are plotted in light gray. (c) Average pairwise distributions of packaging traces selected for low noise levels (50% of all packaging data; see Supplementary Figures 2 and 3). Color scheme as in (b). (d) The average size of the packaging burst versus [ATP] determined from the periodicity in (c). Error bars are the error in the slope from a linear fit to the peak position. Data collected at 500 μM and 1 mM [ATP] are not shown in (b) and (c) for clarity.

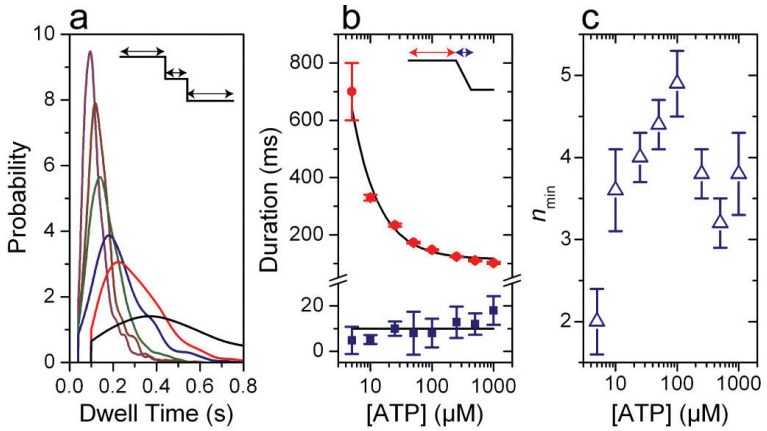

Figure 2. Dwells Before 10-bp Bursts Contain Multiple Kinetic Events

(a) Probability distributions for the dwell times preceding a 10-bp burst under low external load, ∼8 pN, and different [ATP]: color scheme as in Figure 1. Distributions were estimated using kernel density estimation with a Gaussian kernel and the optimum bandwidth46 and are truncated at the lowest detectable dwell time. Supplementary Figure 2 contains the number of observed bursts for each [ATP]. Distributions for 500 μM and 1 mM [ATP] are not shown for clarity. (b) The mean dwell time before the 10-bp bursts (red circles) for all [ATP] with an inverse hyperbolic fit (black) and the mean duration of all bursts (blue squares, average denoted by black line). (c) The minimum number of rate-limiting kinetic events during the dwell before the 10-bp bursts, n_{min}, for all [ATP]. Error bars are the standard error.

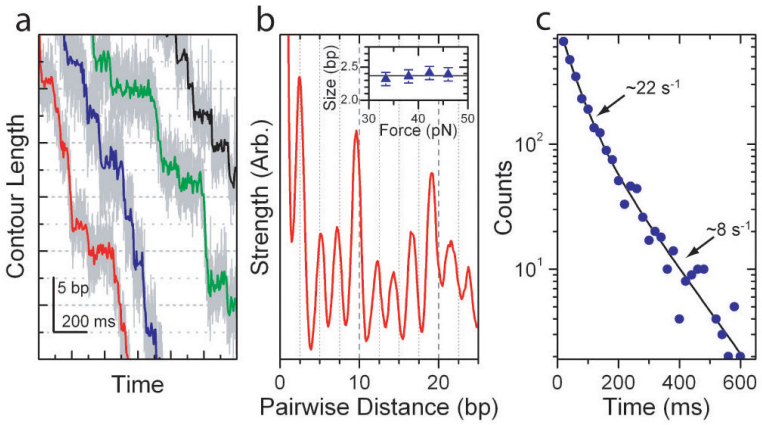

Figure 3. The 10-bp Bursts are Composed of Four 2.5-bp Steps

(a) Representative packaging traces collected with external loads of ∼40 pN and 250 μM [ATP]. Data in light gray are plotted at 1.25 kHz while data in color are boxcar-filtered and decimated to 100 Hz. (b) Average pairwise distribution of packaging traces selected for low noise levels (50% of all packaging data; see Supplementary Figures 2 and 3). Inset: Force dependence of the observed spatial periodicity. The solid line is the mean for all forces 2.4±0.1 bp (s.e.m.). (c) Dwell time histogram for the 2.5-bp steps observed under the packaging conditions seen in (a) plotted in blue circles with a bi-exponential fit in black (N=2,662).

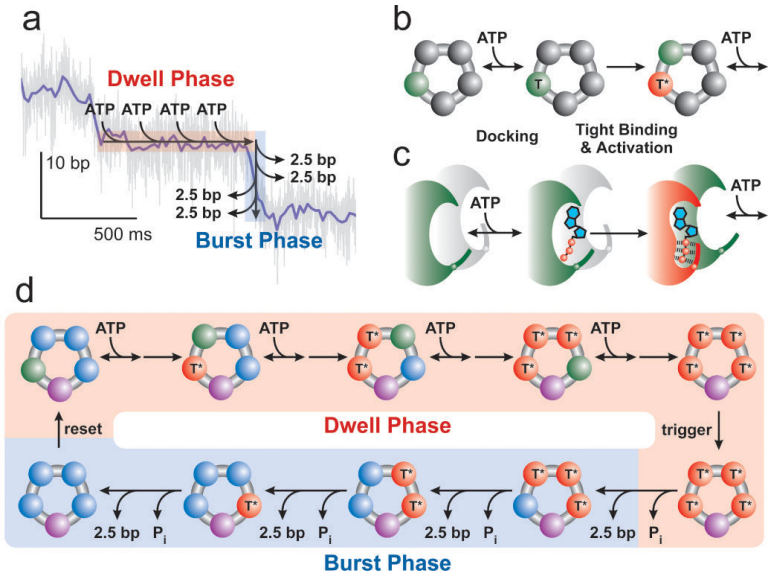

Figure 4. Inter-Subunit Coordination in the Ring-ATPase of ϕ29

(a) Schematic diagram of the two-phase mechanochemical cycle of ϕ29 overlaid on a sample packaging trace. (b) Detailed kinetics of ATP binding. Binding occurs in two steps, ATP docking (green, T) followed by tight-binding (red, T*). (c) Schematic diagram of the communication between subunits during ATP binding. Upon tight-binding of an ATP, the binding pocket of the next subunit, formerly inactive (gray), is activated for docking (green). (d) Schematic depiction of the full mechanochemical cycle of ϕ29. During the burst phase, ADP may remain on the ring (blue) to be released in the dwell phase. One subunit must be distinct from the others (purple) in order to break the symmetry of the motor and generate only 4 steps per cycle. The identity of this subunit may change each cycle.

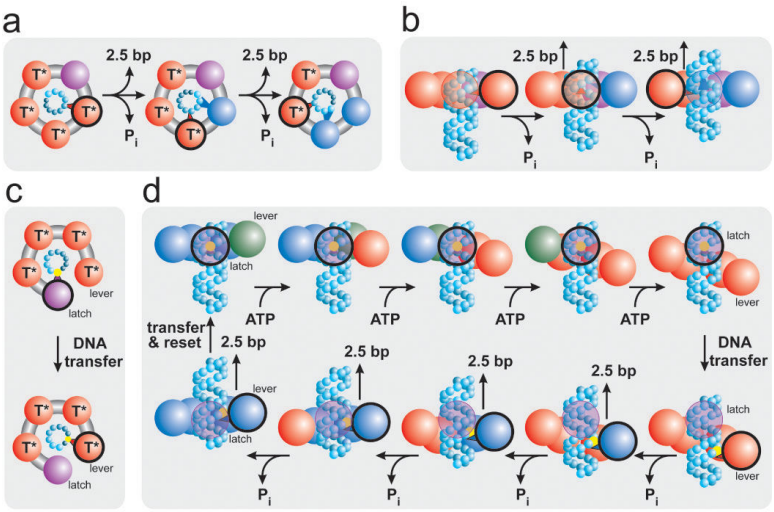

Figure 5. Packaging Models that Produce a Non-Integer Step Size

(a) Depiction of a translocation model in which all subunits eventually contact the DNA (cyan spheres.) The contacting subunit is outlined in black. (b) In such a model the size of internal conformational changes set the step size (side view.) (c) Depiction of a translocation model in which only two subunits contact the DNA (black outline.) (d) In such a model, one subunit maintains contact with the DNA (the latch) while the loading of each ATP introduces relative subunit-subunit rotations which distort the ring. This distortion extends one subunit (the lever) along the DNA by ∼10-bp. The DNA contact point is then transferred from the latch to the lever, and the release of hydrolysis products relaxes the ring, retracting the lever and the DNA. The DNA contact is then transferred back to the latch, the ring resets, and the cycle begins again. Because there are four subunits, the ring is retracted in four steps, dividing a 10-bp step into four ∼2.5-bp substeps. The subunit color scheme is the same as in Figure 4.